

# Magnetic field tuning of crystal field levels and vibronic states in the spin ice compound $\text{Ho}_2\text{Ti}_2\text{O}_7$ observed with far infrared reflectometry

Mykhaylo Ozerov,<sup>1,\*</sup>† Naveen Anand<sup>1,\*</sup>‡ L. J. van de Burgt<sup>2</sup> Zhengguang Lu,<sup>1,3</sup> Jade Holleman,<sup>3,1</sup> Haidong Zhou<sup>1,4</sup>, Steve McGill,<sup>1</sup> and Christianne Beekman<sup>3,1,§</sup>

<sup>1</sup>National High Magnetic Field Laboratory, FSU, Tallahassee, Florida 32310, USA

<sup>2</sup>Department of Chemistry, FSU, Tallahassee, Florida 32306, USA

<sup>3</sup>Department of Physics, FSU, Tallahassee, Florida 32306, USA

<sup>4</sup>University of Tennessee, Knoxville, Tennessee 37996, USA



(Received 22 February 2021; revised 2 March 2022; accepted 3 March 2022; published 1 April 2022)

Low-temperature optical spectroscopy in applied magnetic fields provides clear evidence of magnetoelastic coupling in the spin ice material  $\text{Ho}_2\text{Ti}_2\text{O}_7$ . In far infrared (IR) reflectometry measurements, we observe field-dependent features around 30, 61, 72, and 78 meV, energies corresponding to crystal electronic field (CEF) doublets. The calculations of the crystal field Hamiltonian model confirm that the observed features in IR spectra are consistent with magnetic-dipole-allowed excitations from the ground state to higher  $^5\text{I}_8$  CEF levels. We present the CEF parameters that best describe our field-dependent IR reflectivity measurements. Additionally, we identify a weak field-dependent shoulder near one of the CEF doublets. This indicates that this level is split even in zero field, which we associate with a vibronic bound state. Modeling of the observed splitting shows that the phonon resides at slightly lower energy compared to the CEF level that it couples to, which is in contrast with previously published inelastic neutron measurements. The magnetic field dependence of the vibronic state shows a gradual decoupling of the phonon with the CEF level as it shifts. This approach should work in pyrochlores and other systems that have magnetic dipole transitions in the IR spectroscopic range, which can elucidate the presence and the ability to tune the nature of vibronic states in a wide variety of materials.

DOI: [10.1103/PhysRevB.105.165102](https://doi.org/10.1103/PhysRevB.105.165102)

## I. INTRODUCTION

In pyrochlore titanates  $\text{RE}_2\text{Ti}_2\text{O}_7$ , the magnetic  $\text{RE}^{3+}$  ions occupy a lattice of corner-sharing tetrahedra, providing the quintessential framework to study geometrical frustration in three dimensions [1–3]. These systems have been shown to possess a diverse variety of unconventional cooperative magnetic ground states, including spin liquid and spin ice states [4,5]. The canonical spin ices  $\text{Ho}_2\text{Ti}_2\text{O}_7$  (HTO) and  $\text{Dy}_2\text{Ti}_2\text{O}_7$ , have been studied extensively as they form a two-in/two-out spin configuration on each tetrahedron below  $\theta_W \sim 2$  K [6–8]. This is the result of the very large Ising anisotropy and the long-range dipolar interactions that lead to effective ferromagnetic coupling between  $\text{Ho}^{3+}$  spins [7–9]. Moreover, a large body of recent works have shown that spin ice materials host fractionalized excitations (magnetic monopoles) [10–12].

The localized spin momentum on the  $\text{Ho}^{3+}$  is strongly coupled with the  $4f$  orbital momentum and the interaction of the  $4f$  charge cloud with the crystal electronic field (CEF) from surrounding oxygens leads to the Ising anisotropy found in spin ice materials. As pointed out by Ruminy *et al.*, the CEF Hamiltonian is essential to quantify possible quantum

corrections to the classical model [13] in spin ices like HTO. It explains several intriguing phenomena in the rare-earth pyrochlore systems, i.e., the size of the monopole charge, anisotropy of the magnetic moment, interactions with other degrees of freedom such as phonons and spins [14,15], and coupling strength of any transverse spin component. This provides a logical pathway to understand the mechanism of Ising moment reversal allowing monopole dynamics and quantum fluctuations beyond the classical spin ice limits [16,17]. Considerable activity has been devoted to the determination of the crystal field parameters and the corresponding energy-level scheme in HTO [13,18–21]. Rosenkranz *et al.* obtained the set of six crystal field parameters based on fitting energies of five CEF transitions measured in an inelastic neutron scattering (INS) experiment. Because the number of the observed CEF transitions was restricted, Bertin *et al.* suggested a global fitting procedure based on scaling the energy levels available at that time for a variety of rare-earth ions within the same pyrochlore  $\text{RE}_2\text{Ti}_2\text{O}_7$  series [21]. Recently, two detailed experimental INS studies [13,20] resolved additional CEF transitions in HTO and included the peak intensities into the fitting. However, there is still some discrepancy in these results. While it has been discussed before that magnetic field can be used to resolve some of the discrepancy [21,22], our modeling shows that in order to unambiguously determine the CEF parameters the direction of the magnetic field within the local  $\text{Ho}^{3+}$  ion coordinate frame is an important parameter.

\*These authors contributed equally to this work.

†ozеров@magnet.fsu.edu

‡anand@magnet.fsu.edu

§beekman@magnet.fsu.edu

Magnetoelastic effects are relevant in rare-earth pyrochlores and manifest in terms of modified magnetic, vibrational, and electronic properties [23]. This effect has been recently reported in HTO through INS measurements [20]. The measurements showed that the  $E_g$  CEF doublet around 60 meV was split due to the coupling with a phonon, evidencing the presence of an entangled phononic crystal field excitation due to strong magnetoelastic coupling [20]. As we will show, magnetoinfrared spectroscopy is a powerful tool that can provide insight into CEF transitions and magnetoelastic effects [24–28] in materials with rather complex CEF schemes, such as HTO. Vibronic states have also been observed recently in other pyrochlore titanates [22,29] in the terahertz spectral range. These magneto-optical studies provide a straightforward way to study how CEF-phonon coupling strengths can be varied as a function of applied magnetic field. This work has relevance beyond the pyrochlores. Magnetoinfrared spectroscopy could provide deeper insights into vibronic states observed in other systems, such as the high- $T_C$  superconductor  $\text{NdBa}_2\text{Cu}_3\text{O}_{7-\delta}$ . In this superconductor CEF-phonon coupling can be tuned via isotopic substitution of oxygen (to shift the phonon energy) and by applied fields (to shift the CEF levels), providing two ways to tune the nature of the bound state [30].

The main results presented in this paper are as follows: (1) The observation and modeling of magnetic-dipole-allowed transitions between CEF levels and their evolution in applied magnetic field using far infrared (IR) reflectivity measurements. We found good agreement between the modeling and our data. (2) Finding and modeling the magnetic field dependence of a spectroscopic feature associated with a CEF-phonon coupled (vibronic) state. We modeled the field evolution of the CEF levels and of the vibron using a phenomenological model. The qualitative comparison between the model and the data allows us to estimate CEF parameters, along with the energy of the phonon that couples to the CEF level. Our work is unique in that it uses IR reflectivity rather than transmission and we show that with IR reflectivity it is possible to observe magnetic-dipole-allowed transitions between CEF levels and identify the presence of a vibronic state in HTO. There are many works that describe the CEF levels in HTO, but these are mainly neutron studies, where much larger samples are needed and studying magnetic field dependencies (strength and direction) is time consuming and far from trivial. Interestingly, the field dependence has allowed us to clarify that the specific signs of certain CEF parameters can only be distinguished when the field is applied out of the (110) plane and away from the  $\langle 001 \rangle$  direction in the local  $\text{Ho}^{3+}$  ion coordinate frame (see Supplemental Material [31]). Otherwise, this sign issue will go wholly unnoticed. Furthermore, the magnetic field dependence of the vibronic state shows a gradual decoupling of the phonon with the CEF level as it shifts, which has not been reported before. This approach should work in pyrochlores and other systems that have magnetic dipole transitions in the IR spectroscopic range, which can elucidate the presence and the ability to tune the nature of vibronic states in a wide variety of materials.

This paper is organized as follows. We start with details on the experimental (Sec. II) setup and important information on the procedure for background correction so that small

magnetic-field-induced changes can be extracted. In Sec. III we cover the results, the modeling, and we discuss the significance of our observations. We start with an overview of the data after which we discuss the modeling of our data. We divide the description and discussion of the modeling in subsections, starting with Sec. III A about the zero-field transitions and compare our observations to those reported by others, Sec. III B about the field dependence of the CEF transitions, and lastly Sec. III C about the observation and modeling of the vibronic state in IR reflectivity.

## II. EXPERIMENTAL SETUP

The single-crystal samples of HTO were grown using the optical floating-zone method. The  $\text{Ho}_2\text{O}_3$  and  $\text{TiO}_2$  powders were mixed in a stoichiometric ratio and then annealed in air at 1450 °C for 40 h before growth in an image furnace. The growth was achieved with a pulling speed of 6 mm/h under 5 atm oxygen pressure. The crystals were oriented by Laue back diffraction. The structural and compositional analyses of these samples were performed previously, confirming the cubic symmetry of crystals with the lattice parameter, in agreement with previously reported values [5] (see [6] for more details).

The magnetoinfrared spectroscopy was performed at the National High Magnetic Field Laboratory employing a 17-T vertical-bore superconducting magnet coupled with Fourier-transform infrared spectrometer Bruker Vertex 80v. The collimated IR radiation was propagated from the spectrometer to the top of the magnet inside the evacuated ( $\approx 4$  mBar) optical beamline and then focused to the brass light pipe, used to guide the IR radiation down to the sample space of the magnet. The parabolic 90° mirror focused the IR radiation on the sample with  $\approx 30^\circ$  incident angle, while a second confocal mirror collected the reflected IR radiation inside the twin light pipe with the Si composite bolometer at the end. The reflective surface of the sample was oriented parallel (Voigt geometry) to the magnetic field applied along [001] crystallographic direction. The reflection spectra were measured in the spectral range between 50 and 800  $\text{cm}^{-1}$  with instrumental resolution of 0.3  $\text{cm}^{-1}$ . Both sample and detector were cooled by low-pressure helium gas to a temperature of 5 K. The experimental information about Raman is discussed in the Supplemental Material [31].

The signal-to-noise ratio of the magnetoinfrared data was improved by averaging over three spectra collected at every field point. Then, the single-beam spectrum at each magnetic field was divided by a reference spectrum to remove a strong nonmagnetic background signal and thereby to disclose the tiny field-dependent features. The spectra measured at all magnetic fields were combined into the two-dimensional (2D) matrix, with rows and columns corresponding to energy and magnetic field points, respectively. The reference spectrum is created by taking the highest value of the intensity at each column (i.e., at each frequency point) of this 2D spectrum. The normalization on such statistically created baseline keeps the relative reflectance spectrum below 100% and quantifies the field-induced changes in the reflection signal. The statistical approach for the background correction is frequently used to process transmission data and causes the

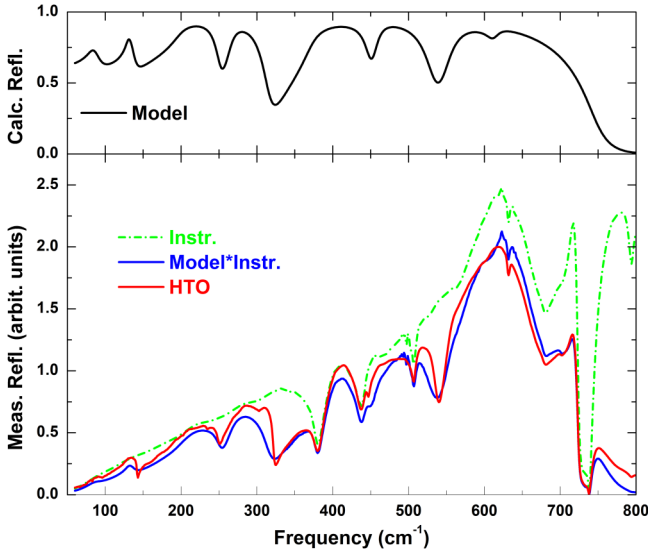


FIG. 1. (Top) Calculated reflectance of HTO after adjusting the parameters from previously published IR studies on  $\text{Dy}_2\text{Ti}_2\text{O}_7$  single crystals [32] to best approximate our measurements (see Table I in the Supplemental Material [31]). (Bottom) Measured single-beam reflected intensity profiles for HTO (red) and a gold reference sample (green). The blue curve shows the multiplication of the model-based calculated reflectance (black) and the gold reference (green).

field-dependent feature to possess a peak line shape, instead of the peak-derivative shape, intrinsic to the normalization on the zero-field spectrum. For instance, Amelin *et al.* [22] employed the approach in their THz transmission study of CEF excitations in another pyrochlore compound  $\text{Tb}_2\text{Ti}_2\text{O}_7$ . Interestingly, this approach also works very well for the analysis of the reflection data presented in this paper.

### III. RESULTS AND DISCUSSION

In Fig. 1 we show single-beam reflected intensities collected for HTO (red curve) and for a gold standard (green dashed curve), taken under similar instrumental conditions. However, the direct ratio method is not a viable option for extracting the absolute reflectance for HTO due to inevitable small mismatches in the optical path and hence the appearance of reflectance values above 100%. Instead, we optimize the previously published Lorentzian parameters for a  $\text{Dy}_2\text{Ti}_2\text{O}_7$  single crystal [32] resulting in a calculated reflectance spectrum (black curve, top panel in Fig. 1). We scale the gold standard intensity profile with this calculated reflectance and superimpose the result over the measured

reflected intensity profile for HTO (blue curve, bottom panel). The comparison between the experimental intensity profile and the model-based calculated reflection intensity profile shows good agreement in the entire frequency range of our interest. While the resonance frequencies barely differ from  $\text{Dy}_2\text{Ti}_2\text{O}_7$  vibrational spectra, the linewidth and oscillator strength for a few phonons show slight variations for HTO. We provide a table in the Supplemental Material [31] listing all the transverse and longitudinal modes used to calculate the reflectance curve.

The relative changes of the IR spectrum induced by applied magnetic field are shown in Fig. 2(b). The magnetic field in our study is applied along the [001] crystallographic direction, which provides the largest net magnetic moment projection and the same CEF level splitting for all four crystallographically different  $\text{Ho}^{3+}$  sites [31]. The significant field-induced responses are found at energies of 30 (visible in 10-T spectrum), 61, 72 (visible in 10-T spectrum), and 78 meV. These energies are in line with previous INS studies [13,19,20] and we can associate these features with CEF excitations from the ground-state doublet  $E_g(0)$  to higher-energy states, shown in Fig. 2(a).

The largest change in the IR reflection spectra is located in the vicinity of 60 meV, that corresponds to the strongest peak in the INS intensity spectrum measured in zero magnetic field and at low temperature [20]. This INS peak appears to have a satellite peak with smaller intensity at the low-energy side. Such splitting is explained by phonon and  $E_g(3)$  CEF level hybridization [20]. Concurrently, the strongest feature of the normalized IR reflection is also different to other peaklike features due to the presence of a shoulder on the low-energy side [see Fig. 2(c)]. Moreover, the shoulder disappears quickly in applied fields of a few Tesla and we will discuss such behavior in more detail in the text below.

Interestingly, we can roughly compare the strength of the electric and magnetic dipole excitations in HTO. While the IR-active phonons induce changes of  $>25\%$  to the ideal 100% reflectivity (Fig. 1), the intensity changes of CEF transitions are about 0.2%–1% of the magnitude of the normalized reflectivity [Fig. 2(b)]. Owing to the high sensitivity of the magnetoinfrared spectroscopy technique, the weak magnetic dipole transitions can be still detected in the broadband spectral range. This enables us to investigate the evolution of CEF levels with applied magnetic field in a straightforward way using far IR reflection measurements, in addition to the magnetoinfrared transmission studies, which are restricted in the spectral range by the transparency windows of the sample. The complete 2D (vs field and energy) spectrum of normalized reflection is presented in Fig. 3, top panel.

TABLE I. Summary of CEF coefficients (in meV) taken from Refs. [13,18–21] and determined in this work.

	$B_2^0$	$B_4^0$	$B_4^3$	$B_6^0$	$B_6^3$	$B_6^6$
Ref. [18]	$-7.6e^{-2}$	$-1.1e^{-3}$	$8.2e^{-3}$	$-7.0e^{-6}$	$-1.0e^{-4}$	$-1.3e^{-4}$
Ref. [21]	$-6.8e^{-2}$	$-1.13e^{-3}$	$-1.01e^{-2}$	$-7.4e^{-6}$	$1.23e^{-4}$	$-1.01e^{-4}$
Refs. [20,35]	$-8.181e^{-2}$	$-1.153e^{-3}$	$-8.175e^{-3}$	$-6.87e^{-6}$	$1.021e^{-4}$	$-1.309e^{-4}$
LS coupling [13]	$-7.811e^{-2}$	$-1.17e^{-3}$	$-8.03e^{-3}$	$-7.07e^{-6}$	$1.03e^{-4}$	$-1.33e^{-4}$
This work	$-7.558e^{-2}$	$-1.156e^{-3}$	$-8.685e^{-3}$	$-7.3e^{-6}$	$1.060e^{-4}$	$-1.264e^{-4}$

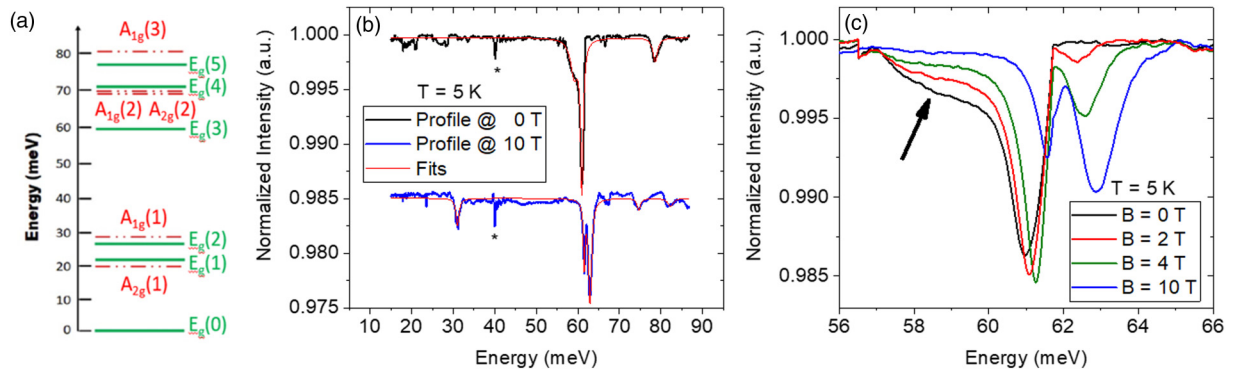


FIG. 2. (a) Schematic showing the CEF energy levels [19] for the  $\text{Ho}^{3+}$  ion in  $\text{Ho}_2\text{Ti}_2\text{O}_7$ . The green solid levels are the  $E_g$  doublets and the red dashed levels are the  $A_{1g}$  and  $A_{2g}$  singlets, respectively. (b) Normalized reflection spectra measured for magnetic fields of  $B = 0$  T (black line) and  $B = 10$  T (blue line, with added offset). The red line is a cumulative fit of three Lorentz peaks at 59.11, 60.96, and 78.60 meV, respectively. An instrumental artifact is marked by the asterisk. (c) Normalized spectra at several magnetic fields in the vicinity of 60 meV. The arrow shows the shoulder slightly below the strongest CEF transition.

### A. CEF Hamiltonian, an overview of zero-field CEF parameters

The pyrochlore compound  $\text{Ho}_2\text{Ti}_2\text{O}_7$  belongs to the cubic space group  $Fd\bar{3}m$ , where the  $\text{Ho}^{3+}$  ions are sitting on sites of

antiprismatic trigonal symmetry  $D3d$  [18]. Hence, the crystal field Hamiltonian in applied magnetic field can be conveniently expressed as the sum of seven terms [18,20,21] as

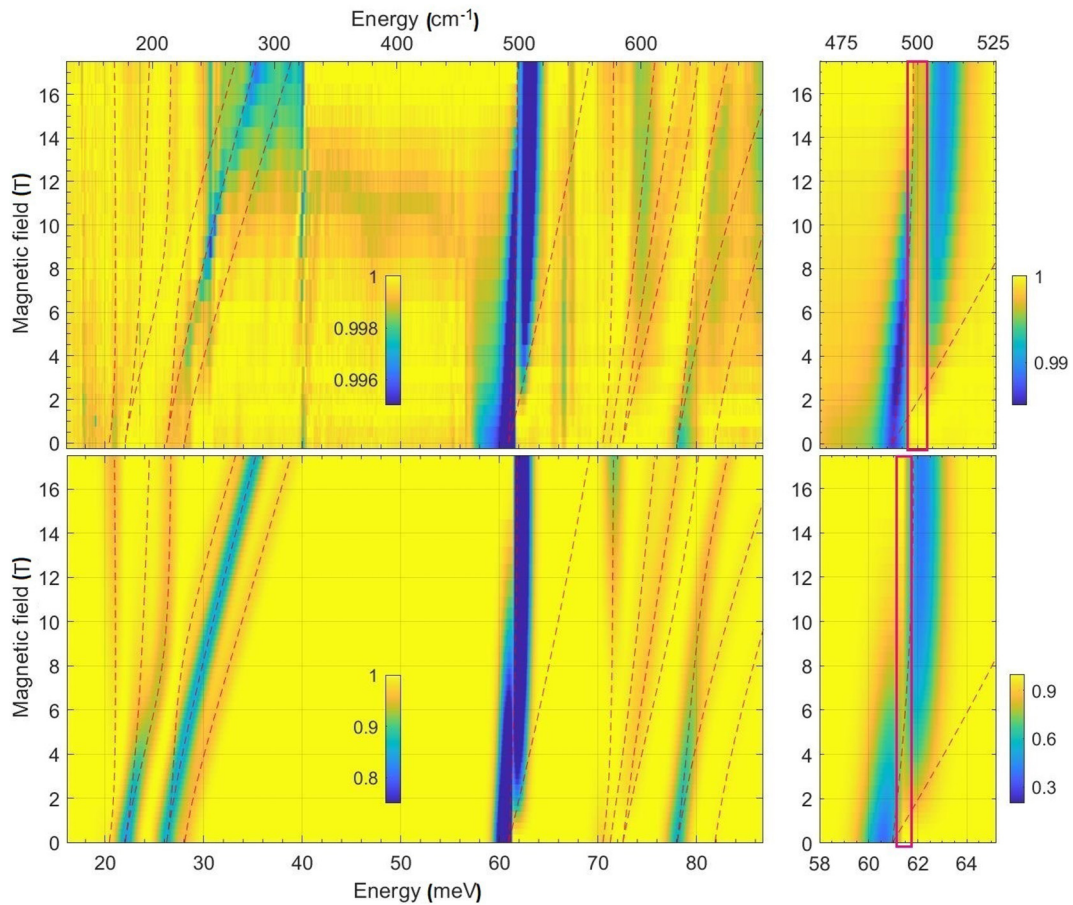


FIG. 3. (Top) The normalized far IR reflection spectrum as a function of the applied magnetic field. (Bottom) The simulation of the transition intensity between ground and high-energy CEF levels. The field dependencies of the transition energy are plotted with red dashed lines. The calculations used CEF parameters presented in the bottom row of Table I. Both experimental and calculated spectra were normalized to the reference spectrum obtained from the statistical approach described in the text, respectively. The panels on the right show field evolution of the strongest CEF transition in the vicinity of 61 meV. The boxed region in both panels shows the artifact due to the normalization procedure.

TABLE II. The experimentally observed and calculated CEF energies in  $\text{Ho}_2\text{Ti}_2\text{O}_7$  (meV) at zero magnetic field.

CEF	$E_{\text{obs}}$ [20]	$I_{\text{obs}}$ [20]	$E_{\text{obs}}$ [13]	$I_{\text{obs}}$ [13]	$E_{\text{cal}}$
$E_g$	0	0	0	0	0
$A_{2g}$	20.7	0.03			20.42
$E_g$	22	0.19	21.9	0.2	22.024
$E_g$	26.3	0.17	26.3	0.14	26.24
$A_{1g}$	28.4	0.03	28.3	0.02	28.07
$E_g$	58.9	1	61.0	1	60.96
$A_{1g}$					70.51
$A_{2g}$	71.2	0.05			71.26
$E_g$			72(1)	0.08	72.55
$E_g$	77.9	0.12	78.7	0.1	78.05
$A_{1g}$					81.89

$$\mathcal{H}_{\text{CEF}} = B_2^0 \hat{O}_2^0 + B_4^0 \hat{O}_4^0 + B_4^3 \hat{O}_4^3 + B_6^0 \hat{O}_6^0 + B_6^3 \hat{O}_6^3 + B_6^6 \hat{O}_6^6 + g_L \hat{J}H, \quad (1)$$

where  $\hat{O}_k^q$  are the extended Stevens operators and  $B_k^q$  are the associated coefficients. The last term is the Zeeman energy defined by the Lande  $g$  factor  $g_L = \frac{5}{4}$ , angular momentum operator  $\hat{J}$  ( $|J| = 8$ ), and the magnetic field  $H$ , applied along  $\langle 111 \rangle$  axis in the local  $\text{Ho}^{3+}$  coordinate frame ( $[001]$  direction in the laboratory frame) [31]. We solved this problem and calculated the intensity of magnetic-dipole-allowed transitions at  $T = 0$  K using the EASYS PIN package [33,34] in MATLAB.

There are several prior studies that report values for the CEF parameters  $B_k^q$ . Rosenkranz *et al.* [19] report the parameters determined from transition energies observed in INS experiments. Recently, two detailed experimental INS studies [13,20] clearly resolved CEF transitions in HTO and, furthermore, allowed to include their relative intensities into the fit constraints. Although Gaudet *et al.* [20] observed the most intensive peak at 61 meV, it was concluded that the corresponding CEF transition was at 58.9 meV. Such redshift was attributed to the hybridization of  $E_g$  level with the silent phonon via vibronic coupling. Using Stevens renormalization procedure [36] we reproduce the CEF parameters from Bertin *et al.* [21], Rosenkranz *et al.* [19] (same as Tomasello *et al.* [18]), Gaudet *et al.* [20], and Ruminy *et al.* (LS-coupling scheme [13]) in Table I. The main differences between all of these sets are (i) the sign of the coefficients  $B_4^3$  and  $B_6^3$ , and (ii) a relatively large spread ( $\sim 20\%$ ) in most of the  $B_k^q$  values also becomes apparent.

The CEF excitation spectra were simulated for zero magnetic field for each of the parameter sets shown in Table I are shown in Fig. 4, along with the intensities of the experimentally observed INS peaks (Table II). The simulation deviates from the observed values (see Fig. 4), which is related to complexity of multiple-parameter fitting as well as to the discrepancy in the peak assignment. The simulated CEF excitation spectrum using CEF parameters from Tomasello *et al.* [18,19] [Fig. 4(a)] does not agree with the INS results from Ruminy *et al.* [13]. Similar deviations are found when comparing the CEF excitation spectrum using Bertin *et al.* [21] CEF parameters [Fig. 4(b)]. In Fig. 4(c) of the same figure, the simulated spectrum using the LS-coupling

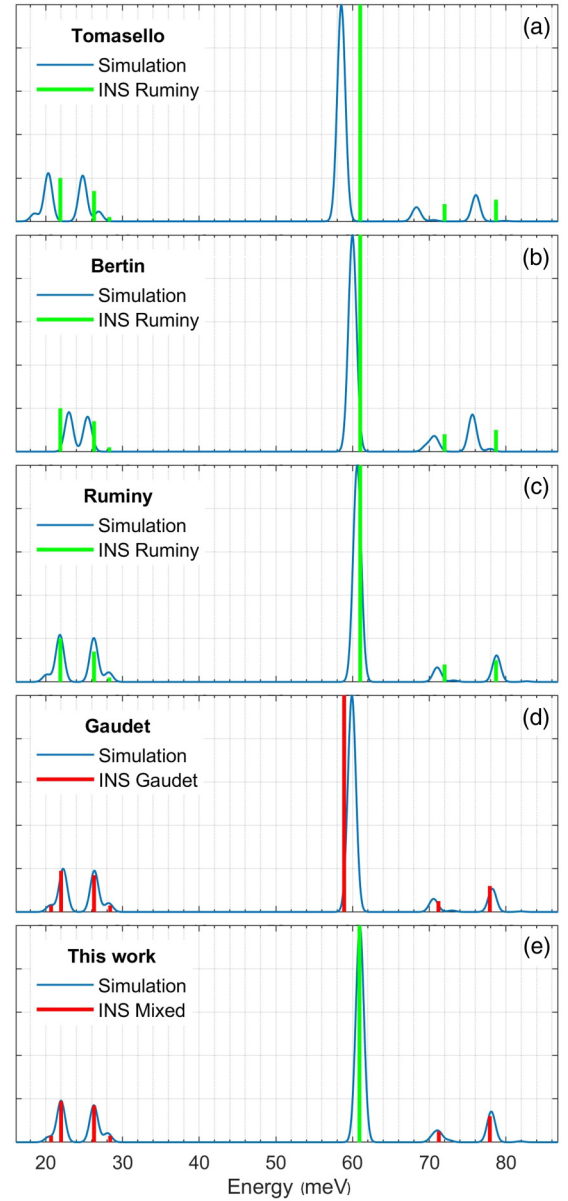


FIG. 4. Zero-field CEF excitation spectrum observed by INS studies (green bars [13] and red bars [20]). The blue lines are simulations of CEF transitions using Hamiltonian in Eq. (1) and Stevens coefficients shown in Table I.

CEF parameters [13] is compared to the INS observations and overall the agreement is good. Lastly [Ref. [20] and Fig. 4(d)], the position of the strongest peak observed in the INS experimental spectrum is different compared to the calculated nominal energy of the  $E_g(0) \rightarrow E_g(3)$  transition based on the presented CEF parameter values.

Ideally, we would simulate a similar zero-field spectrum solely based on our IR spectroscopy results. However, given that we only observe two of the expected seven transitions in zero applied field, this would not produce reliable CEF parameter values. Hence, we adopt the following optimization approach: we use reported INS data (Table II) that most closely matches our IR spectroscopy data and fit both energies and intensities of INS peaks using CEF Hamiltonian (1) in

zero field [Fig. 4(e)]. The obtained CEF parameter values that best reproduce those transition energies and intensities are further used for simulations with applied fields without any other adjustments.

Note, these optimized CEF parameters are considerably different from previously reported values for three main reasons: (1) The spread in the observed transition energy for  $E_g(3)$ , for optimization we selected 61 meV for this transition, in line with our IR spectroscopy data and most closely matching the transition energy reported by Ruminy *et al.* [13] (see Table II). (2) The simulations based on previously reported CEF parameter values show a mismatch when compared to the reported observed CEF transition energies. (3) The reported CEF parameter values consistently underestimate the observed transition energy that occurs around 70 meV, which is likely a sum of the  $E_g(4)$  and  $A_{2g}$  transitions. To give a sense of how CEF parameters affect the transition energies, we show the shift of each of the CEF levels (about 1 meV) for a 5% variation of each of the CEF parameters (see Supplemental Material [31]).

### B. Modeling of field-dependent IR reflectivity data

We use the optimized zero-field  $B_k^q$  coefficients (last row in Table I) to model the field dependence of the CEF transitions and to compare it with experimental observations. The top panel of Fig. 3 shows the color map of measured intensities as determined from magnetoinfrared reflection spectroscopy, along with the calculated Zeeman splitting of the CEF levels (red lines). The data exhibit a very good agreement with the shifts in the calculated CEF transitions for  $E_g(2)$  (at  $\approx 26$  meV in zero field),  $E_g(3)$  (at  $\approx 61$  meV in zero field), and  $E_g(5)$  (at  $\approx 78$  meV in zero field). This agreement is striking, as the simulated intensity is appropriate for transmission experiments, while our IR spectra are measured in a reflection geometry. Our measurements do not show a clear transition associated with the two lowest-energy CEF levels around 20 meV. This is due to low sensitivity of our measurement in this energy range. Furthermore, at low field, the IR transitions will be prone to thermal broadening, making them harder to observe and model. It appears that a field of 5 T or greater is needed to resolve some weaker features in the IR spectra.

It is worth to note that zero-field INS spectra can be equally fitted with two sets of the CEF coefficients, with the difference being the sign of the  $B_4^3$  and  $B_6^3$  coefficients. The sign of these coefficients does alter the magnetic field induced splitting of some CEF levels, but how the transition energies are affected depends on the direction of the magnetic field within the crystal field frame [31]. With the field applied in the  $xy$  plane [18] or along the  $z$  axis in the  $\text{Ho}^{3+}$  local frame, the resultant transition energies appear invariant upon a sign change of the  $B_4^3$  and  $B_6^3$  coefficients. Only if the field is applied away from these directions, like along one of the  $\langle 111 \rangle$  axes (which is the case in our experiment), the transition energy becomes sensitive to this sign change (see Supplemental Material [31]). In agreement with a previous paper for  $\text{Tb}_2\text{Ti}_2\text{O}_7$  [22], we experimentally distinguished signs of the CEF parameters in HTO using applied magnetic fields (Fig. S13 in Supplemental Material [31]). Furthermore, if we use the previously reported Stevens coefficients (see Table I) and calculate the field

dependence of the CEF levels, we find the agreement with our IR data to be far less [31]. This shows that magnetoinfrared is effective in characterizing the field dependence of CEF levels and that some Stevens operators can be determined with a greater degree of accuracy, at least compared to zero-field measurements using other probes.

To further compare our optimized CEF parameters to previously reported values, we determined and tabulated the wave functions for each of the  $m_J$  values of the ground-state multiplet for all parameters in Table I (see Supplemental Material [31]). Quantum corrections to the classical model [13,17] stem from spectral content of subleading components of the wave function. As expected, we find the spectral content to be predominantly  $|\pm 8\rangle$  with the subleading components of the wave function comparable to those presented by others [13,18,21].

### C. Observation and modeling of vibronic states.

While Eq. (1) satisfactorily describes the splitting of the CEF levels in applied magnetic fields, this model does not explain the appearance of the field-dependent shoulder observed on the low-energy side of the 61-meV transition. This shoulder clearly indicates that this CEF level is split even in zero field. This observation is consistent with previously reported INS measurements [20], which reported evidence of overlapped vibrational and electronic degrees of freedom, resulting in a vibronic bound state around the same doublet transition energy. Density functional theory (DFT) calculations by others [13,37,38] have reported the presence of an optically silent phonon mode of  $E_u$  symmetry in the close vicinity of the  $E_g(3)$  doublet transition. In the following, we will model this behavior and extract an energy for the phonon that results in the observed CEF-phonon hybridization.

To model the shoulder in the vicinity of 61 meV in the IR spectra, we are solving the following Hamiltonian (2), similar to the previous papers [20]:

$$\mathcal{H}_{\text{tot}} = \mathcal{H}_{\text{CEF}} + \hbar\omega(\hat{a}^\dagger\hat{a} + 1/2) - \sum_{q=-2}^{+2} g_q(\hat{a}^\dagger + \hat{a})\widehat{B}_2^q\widehat{O}_2^q. \quad (2)$$

Here,  $\mathcal{H}_{\text{CEF}}$  is the crystal field Hamiltonian with the Zeeman term [Eq. (1)]. The operators  $\hat{a}^\dagger$  and  $\hat{a}$  correspond to the creation and annihilation of a phonon. The last term represents the vibronic Hamiltonian [20,22] with phenomenological coupling constants  $g_q$  and quadrupolar operators  $\widehat{O}_2^q$ . The coupling constants were taken  $g_{\pm 2} = g_0$  and  $g_{\pm 1} = 2g_0$  to provide the same weight for the angular momentum operators as in Ref. [20]. The IR response is proportional to the transition matrix element of the magnetic-dipole operator, which we calculated between the lowest-energy  $E_g(0)$  doublet state and four states, resulting from the coupling of the  $E_g(3)$  doublet and  $E_u$  phonon.

Figure 5(a) shows the intensity associated with the  $E_g(3)$  CEF excitation in the presence of phonon-CEF hybridization, with the phonon energy  $\hbar\omega = 59.5$  meV indicated by the dashed blue line. The red dashed lines are the same as in Fig. 3. The color map clearly indicates the presence of a much broader feature around 61 meV compared to the simulated IR intensity using  $\mathcal{H}_{\text{CEF}}$  alone. To compare to our measured

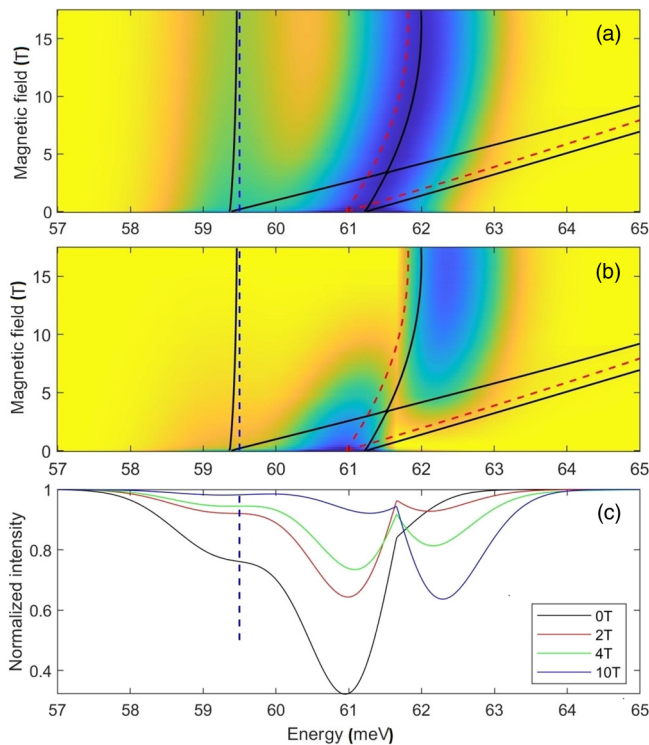


FIG. 5. (a) Illustration of the excitation spectrum from ground to hybridized states as a function of the magnetic field. The intensity of the transitions is calculated for  $T = 0$  K,  $\hbar\omega = 59.5$  meV, coupling constant  $g_0 = 0.016$ , and Lorentzian linewidth of 1.6 meV. The dashed red and blue lines correspond to the  $E_g(3)$  CEF doublet and phonon mode, respectively. The black solid lines show energies of hybridized states. (b) The same excitation spectrum but now normalized by a reference spectrum, calculated in the same way applied for Fig. 3. (c) Profiles taken at various fields based on the middle panel.

data we apply the same normalization routine to the calculated data as before, which results in the color map in Fig. 5(b). Profiles taken at  $B = 0, 2, 4,$  and  $10$  T result in Fig. 5(c) and show the field evolution of the shoulder, disappearing quickly with increasing field strength. The normalization procedure distorts the original Lorentzian line shape and introduces a kink around 61.5 meV manifesting as a vertical yellow strip between two bluish areas [Fig. 5(b)]. This artifact is also observed in the experimental data (Fig. 3, right panels) and stems from the considerable linewidth, which is larger than the field-induced shift of the peak position. Assuming the phonon energy just below the CEF level, we obtain a field evolution that is in great agreement with our data. We repeated the simulation for a phonon energy that lies above the CEF level and get a completely different result, i.e., the shoulder would appear on the high-energy side of the CEF transition (see Supplemental Material for more details). We conclude, unlike what was reported in Gaudet *et al.* [20], that the phonon

energy has to be lower than the CEF transition energy in order to get the observed response in IR spectroscopy.

Finally, it is worth noting that Hamiltonian (2) is just an approximation, allowing to qualitatively and semiquantitatively describe our findings and explain why the vibronic shoulder shows up in our IR data for low magnetic fields only. For instance, the atomic displacements of the phonon mode have a complex influence to the crystal field of  $\text{Ho}^{3+}$  ions and, hence, each quadrupole operator  $\tilde{B}_2^q$  would have different coupling constant  $g_q$ . In addition, the presence of the vibronic coupling leads to some intensity on the fast-moving CEF branch associated with  $E_g(3)$  transition, while only the transition to the lower  $E_g(3)$  doublet branch is magnetic-dipole allowed for  $g_0 = 0$ . In our experiment, the intensity of the higher-lying branch might be obscured for low fields by the high intensity of the slow-moving CEF branch, while for higher fields, its intensity is already disappeared as the phonon decouples from the CEF level as the field is increased (see Supplemental Material [31] for more details).

#### IV. CONCLUSIONS

We have investigated the broadband magneto-optical response of HTO single crystals as a function of applied magnetic field. The weak magnetic-dipole excitations between CEF levels were revealed in the far IR reflection signal on top of the strong electric-dipole phonon excitations. We model our magnetoinfrared spectra using the crystal field Hamiltonian and a Zeeman term, leading to very good agreement with experimental observations. Our results unambiguously determine the sign of the  $B_4^3$  and  $B_6^3$  coefficients, which is impossible in zero-field measurements. Additionally, our spectroscopic data also clearly show the presence of splitting of the  $E_g(3)$  CEF level at zero field, which we associate with a vibronic state. This vibronic state only appears at low field as its intensity quickly diminishes in applied magnetic fields. Modeling of the observed splitting shows that the phonon resides at slightly lower energy compared to the CEF level that it couples to, which is in contrast with previously published INS results [20].

#### ACKNOWLEDGMENTS

C.B. acknowledges support from the National Research Foundation, under Grant No. NSF DMR-1847887. A portion of this work was performed at the National High Magnetic Field Laboratory, which is supported by National Science Foundation Cooperative Agreements No. DMR-1157490 and No. DMR-1644779, and the State of Florida. H.D.Z acknowledges support from the NHMFL Visiting Scientist Program, which is supported by NSF Cooperative Agreement No. DMR-1157490 and the State of Florida.

[1] A. P. Ramirez, *Annu. Rev. Mater. Sci.* **24**, 453 (1994).

[2] M. J. Harris, S. T. Bramwell, D. F. McMorrow, T. Zeiske, and K. W. Godfrey, *Phys. Rev. Lett.* **79**, 2554 (1997).

[3] M. J. Harris, S. T. Bramwell, P. C. W. Holdsworth, and J. D. M. Champion, *Phys. Rev. Lett.* **81**, 4496 (1998).

[4] J. E. Greedan, *J. Alloys Compd.* **408-412**, 444 (2006).

- [5] J. S. Gardner, M. J. P. Gingras, and J. E. Greedan, *Rev. Mod. Phys.* **82**, 53 (2010).
- [6] K. Barry, B. Zhang, N. Anand, Y. Xin, A. Vailionis, J. Neu, C. Heikes, C. Cochran, H. Zhou, Y. Qiu, W. Ratcliff, T. Siegrist, and C. Beekman, *Phys. Rev. Materials* **3**, 084412 (2019).
- [7] C. R. Wiebe and A. M. Hallas, *APL Mater.* **3**, 041519 (2015).
- [8] H. D. Zhou, J. G. Cheng, A. M. Hallas, C. R. Wiebe, G. Li, L. Balicas, J. S. Zhou, J. B. Goodenough, J. S. Gardner, and E. S. Choi, *Phys. Rev. Lett.* **108**, 207206 (2012).
- [9] B. C. den Hertog and M. J. P. Gingras, *Phys. Rev. Lett.* **84**, 3430 (2000).
- [10] M. J. P. Gingras and P. A. McClarty, *Rep. Prog. Phys.* **77**, 056501 (2014).
- [11] C. Castelnovo, R. Moessner, and S. L. Sondhi, *Nature (London)* **451**, 42 (2008).
- [12] L. D. C. Jaubert and P. C. W. Holdsworth, *J. Phys.: Condens. Matter* **23**, 164222 (2011).
- [13] M. Ruminy, E. Pomjakushina, K. Iida, K. Kamazawa, D. T. Adroja, U. Stuhr, and T. Fennell, *Phys. Rev. B* **94**, 024430 (2016).
- [14] S. Petit, J. Robert, S. Guitteny, P. Bonville, C. Decorse, J. Ollivier, H. Mutka, M. J. P. Gingras, and I. Mirebeau, *Phys. Rev. B* **90**, 060410(R) (2014).
- [15] P. A. McClarty, S. H. Curnoe, and M. J. P. Gingras, *J. Phys.: Conf. Ser.* **145**, 012032 (2009).
- [16] V. Klekovkina and B. Malkin, *Opt. Spectrosc.* **116**, 849 (2014).
- [17] J. G. Rau and M. J. P. Gingras, *Phys. Rev. B* **92**, 144417 (2015).
- [18] B. Tomasello, C. Castelnovo, R. Moessner, and J. Quintanilla, *Phys. Rev. B* **92**, 155120 (2015).
- [19] S. Rosenkranz, A. P. Ramirez, A. Hayashi, R. J. Cava, R. Siddharthan, and B. S. Shastry, *J. Appl. Phys.* **87**, 5914 (2000).
- [20] J. Gaudet, A. M. Hallas, C. R. C. Buhariwalla, G. Sala, M. B. Stone, M. Tachibana, K. Baroudi, R. J. Cava, and B. D. Gaulin, *Phys. Rev. B* **98**, 014419 (2018).
- [21] A. Bertin, Y. Chapuis, P. D. de Réotier, and A. Yaouanc, *J. Phys.: Condens. Matter* **24**, 256003 (2012).
- [22] K. Amelin, Y. Alexanian, U. Nagel, T. Room, J. Robert, J. Debray, V. Simonet, C. Decorse, Z. Wang, R. Ballou, E. Constable, and S. de Brion, *Phys. Rev. B* **102**, 134428 (2020).
- [23] S. Erfanifam, S. Zherlitsyn, S. Yasin, Y. Skourski, J. Wosnitza, A. A. Zvyagin, P. McClarty, R. Moessner, G. Balakrishnan, and O. A. Petrenko, *Phys. Rev. B* **90**, 064409 (2014).
- [24] M. Maćzka, M. L. Sanjuan, A. F. Fuentes, L. Macalik, J. Hanuza, K. Matsuhira, and Z. Hiroi, *Phys. Rev. B* **79**, 214437 (2009).
- [25] S. Jandl, S. Mansouri, J. Vermette, A. A. Mukhin, V. Y. Ivanov, A. Balbashov, and M. Orlita, *J. Phys.: Condens. Matter* **25**, 475403 (2013).
- [26] S. Mansouri, S. Jandl, M. Balli, P. Fournier, A. A. Mukhin, V. Y. Ivanov, A. Balbashov, and M. Orlita, *J. Phys.: Condens. Matter* **30**, 175602 (2018).
- [27] J. Vermette, S. Jandl, M. Orlita, and M. M. Gospodinov, *Phys. Rev. B* **85**, 134445 (2012).
- [28] T. T. A. Lummen, I. P. Handayani, M. C. Donker, D. Fausti, G. Dhahlenne, P. Berthet, A. Revcolevschi, and P. H. M. van Loosdrecht, *Phys. Rev. B* **77**, 214310 (2008).
- [29] E. Constable, R. Ballou, J. Robert, C. Decorse, J.-B. Brubach, P. Roy, E. Lhotel, L. Del-Rey, V. Simonet, S. Petit, and S. deBrion, *Phys. Rev. B* **95**, 020415(R) (2017).
- [30] E. T. Heyen, R. Wegerer, and M. Cardona, *Phys. Rev. Lett.* **67**, 144 (1991).
- [31] See Supplemental Material at <http://link.aps.org/supplemental/10.1103/PhysRevB.105.165102> for room-temperature Raman spectra and resonant Raman spectra (laser line  $\lambda = 532$  nm) as a function of applied field taken at  $T = 5$  K. We present more details regarding the modeling of the observed CEF transitions in IR, by showing the calculated response for the inequivalent  $\text{Ho}^{3+}$  sites, and the field dependence of the CEF levels when using CEF parameters previously reported by others. We present calculated field dependencies of two CEF transitions for various field directions to show how the field direction influences the ability to distinguish signs of CEF coefficients. We present additional simulated IR response of the vibronic state for a phonon energy that lies above the CEF level.
- [32] C. Z. Bi, J. Y. Ma, B. R. Zhao, Z. Tang, D. Yin, C. Z. Li, D. Z. Yao, J. Shi, and X. G. Qiu, *J. Phys.: Condens. Matter* **17**, 5225 (2005).
- [33] S. Stoll and A. Schweiger, *J. Magn. Reson.* **178**, 42 (2006).
- [34] J. Nehr Korn, J. Telsler, K. Holldack, S. Stoll, and A. Schnegg, *J. Phys. Chem. B* **119**, 13816 (2015).
- [35] A. Freeman and J. Desclaux, *J. Magn. Magn. Mater.* **12**, 11 (1979).
- [36] K. W. H. Stevens, *Proc. Phys. Soc. A* **65**, 209 (1952).
- [37] S. Kumar and H. Gupta, *Vib. Spectrosc.* **62**, 180 (2012).
- [38] A. K. Kushwaha, *Int. J. Mod. Phys. B* **31**, 1750145 (2017).